Computational modeling of braided venous stents - effect of design features and device-tissue interaction on stent performance

journal of the mechanical behavior of biomedical materials 142 (2023) 105857

Contents lists available at ScienceDirect

Journal of the Mechanical Behavior of Biomedical Materials

journal homepage: www.elsevier.com/locate/jmbbm

Research paper

Computational modeling of braided venous stents — Effect of design features and device-tissue interaction on stent performance

René Ubachs [a], Olaf van der Sluis [a,b,*], Scott Smith [c], Jake Mertens [c]

[a] Philips Research, High Tech Campus 34, 5656 AE Eindhoven, The Netherlands
[b] Eindhoven University of Technology, Eindhoven, The Netherlands
[c] Philips Image Guided Therapy Devices, 5905 Nathan Lane, Plymouth, MN, United States

ARTICLE INFO

Keywords:
Braided stent
Venous stent
Computational modeling
Self-expanding stent
Design optimization
Finite element analysis
Device-tissue interaction
Stent performance criteria

ABSTRACT

Designing venous stents with desired properties is challenging due to the partly conflicting performance criteria, e.g., enhancing flexibility may be at odds with increasing patency. To evaluate the effect of design parameters on the mechanical performance of braided stents, computational simulations are performed using finite element analysis. Model validation is performed through comparison with measurements. Considered design features are stent length, wire diameter, pick rate, number of wires, and stent end-type, being either open-ended or closed looped. Based on the requirements of venous stents, tests are defined to study the effect of design variations with respect to the following key performance criteria: chronic outward force, crush resistance, conformability, and foreshortening. Computational modeling is demonstrated to be a valuable tool in the design process through its ability of assessing sensitivities of various performance metrics to the design parameters. Additionally, it is shown, using computational modeling, that the interaction between a braided stent and its surrounding anatomy has a significant impact on its performance. Therefore, taking into account device-tissue interaction is crucial for the proper assessment of stent performance.

1. Introduction

The treatment of venous disease and venous stenting is gaining interest in recent years. Stenting may be performed to recanalize a vessel and maintain patency or to provide crush resistance against external loadings such as is the case for the May–Thurner syndrome (May and Thurner, 1957). Another desirable characteristics of a venous stent is accurate deployment, i.e., the stent lands at the intended position and spans the intended length. Both these requirements are influenced by foreshortening, the reduction of stent length during radial expansion.

Braided stents, particularly the Wallstent™ (Boston Scientific Corporation), have shown to be suited candidates in the veinous space (Ye et al., 2012; Murphy, 2019). They provide excellent fatigue resistance, good radial outward force and crush resistance, and are capable of following the contours of curved vessels, i.e., showing good conformability. Shortcomings of the Wallstent are its significant foreshortening and the weakness of the open ends of the stent which are prone to collapse and fish mouthing, potentially leading to re-occlusion.

Analytical models to calculate the response of braided stents to idealized loading conditions are available in literature (Jedwab and Clerc, 1993; Wang and Ravi-Chandar, 2004a,b; Loo, 2006; Zaccaria et al., 2021). Although these analytical models have the advantage of providing insights rapidly and clearly, their use is limited to idealized configurations and one must always be mindful of the assumptions used to derive the equations.

A more generic approach is the use of numerical methods, e.g., the finite element method. Instead of using a full 3D solid model which would require a very high number of elements, a common approach for modeling braided stents is the use of 1D beam elements (Conti, 2007; Záhora et al., 2007; Auricchio et al., 2011). This results in a much more computationally efficient approach than 3D solid elements. Another big hurdle for the finite element approach is the description of the wire crossovers. Due to the multitude of and continuously changing wire-to-wire contacts, numerical challenges arise during the simulation which decrease the model's efficiency. Using a contact method to describe this is the most general approach, imposing no artificial restrictions. However, this will give rise to poor convergence due to the inherent nonlinearities associated with contact algorithms. Simplified ways of describing the interactions are therefore often employed where the contact is replaced by some kind of connection between neighboring nodes of touching wires. With the join method, used by Conti (2007), Auricchio et al. (2011), relative displacement between the tied nodes is constraint while relative rotation is allowed. With the hinge method, as

* Corresponding author at: Eindhoven University of Technology, Eindhoven, The Netherlands.
E-mail address: o.v.d.sluis@tue.nl (Olaf van der Sluis).

https://doi.org/10.1016/j.jmbbm.2023.105857
Received 19 January 2023; Received in revised form 25 March 2023; Accepted 12 April 2023
Available online 20 April 2023

used by Shanahan et al. (2017b), the join connector is combined with a revolute connector, which enables a revolute connection between rotational degrees of freedom. Ma et al. (2012) show that taking into account inter-wire contact and friction for an in silico study is feasible. They model the entire stent deployment process of braided stents in patient specific cerebral vasculature using the general contact algorithm Abaqus/Explicit. Zaccaria et al. (2020) evaluate the hinge and join description of the inter-wire contact taking the general contact algorithm as a reference standard. They conclude that although the simplifications of the contact description allow for the use of an implicit solver, the results of the connector models are strongly influenced by wire interpenetrations and over-constraint and therefore the contact option is the best and preferred choice.

Braided stents come in two major versions, open-ended and closed-looped. Shanahan et al. (2017a) compare the difference between these version using finite element simulations and comparing with a corrected version of the analytical work of Jedwab and Clerc (1993). The contact between the wires is described by hinge connectors in the finite element software package Abaqus. They note the importance of the looped ends on the magnitude of the radial forces.

Friction between the wires has been shown to play an important role in the behavior of braided stents (Wang and Ravi-Chandar, 2004b). Giuliodori et al. (2021) perform simulations on covered braided stents using beam elements and describing the wire-to-wire interactions with the join method. Axial tension springs at crossover locations are introduced to account for the added stiffness of the polymeric covering. Additionally, friction between the wires is accounted for by torsion springs at crossover points between the wires, thus negating one of the shortcomings of the connector element approach. Kim et al. (2008) model a braided stent in Abaqus/Explicit using contact between the braided wires. They investigate the effect of braiding angle and number of wires. In addition, they study the effect of hysteresis caused by friction between the wires.

In this paper computational simulations using finite element analysis to evaluate the effect of design parameters on the mechanical performance of venous braided stents are presented. Currently, sufficient high quality in-vitro and in-vivo data for venous stents are not yet available as this is a relatively new field. To extract meaningful information from these simulations, the approach is as follows: we use in-vitro bench and in-silico test results to compare performance criteria to existing designs which are known to be safe, e.g., the wall stent. Specifically, we use the radial crimp test to determine chronic outward forces and foreshortening, cylinder and stent-end crush for crush resistance, and stent deployment in a bent tube for conformability. Comparing performance data of these designs to existing stents is a valid approach as the performance and safety of these stents is well established and can thus be considered as reference. When more data on venous stentings become available, it is anticipated that computational models could be used to correlate clinical endpoints to detailed stent performance criteria as obtained from the simulations.

Since describing the interaction between the wires in a simplified manner can under certain conditions lead to unphysical behavior (Zaccaria et al., 2020), here it is modeled using a contact algorithm. The finite element model is validated by comparing computational with bench testing results. Subsequently, computational modeling and simulation is used to quantify the effect of stent design features on relevant stent performance metrics such as conformability, chronic outward force and crush resistance, where a distinction is made between unrestricted bench tests and the performance when deployed in a vein. The results are analyzed, and feature-performance correlations are presented. Finally, the significant differences between performance characterization tests on unrestricted stents and on stents in a more realistic surroundings, e.g., deployed in a vessel, are analyzed and explained and the importance of accounting for device-tissue interaction is demonstrated.

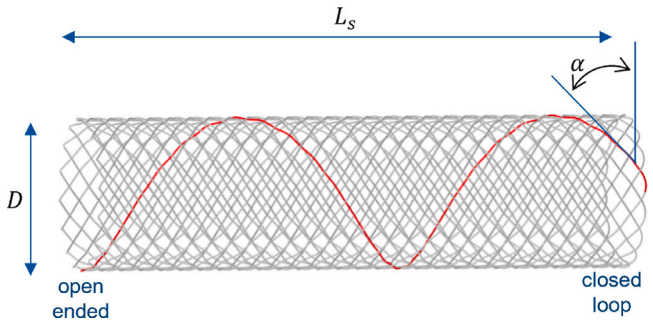

Fig. 1. Beam model of braided stent. D is the stent diameter, L_s its length and α the pitch angle.

2. Computational stent models

2.1. Braided stent

A Python script using parametric equations, see Appendix, is used to create finite element models of the braided stents. The variables available in the script are the number of wires, N, wire diameter, d, stent length, L_s, stent diameter, D, picks per inch, P, stent end type. The pick rate is the number of crossovers per inch of axial length of the stent. Together with the number of wires this determines the winding or pitch angle. The stent end type may be looped or open. Fig. 1 shows an example of a braided stent with one looped and one open end, including the used geometry parameters in the equation.

The Abaqus/Explicit solver has been used to perform calculations as it can efficiently deal with the nonlinearities arising from both the material and the large number of mechanical contacts that occur between the wires of the stent. The resulting finite element mesh consists of beam elements, type B31. Typical length of a beam element is 0.5 mm while beam diameters varied from 0.13 to 0.25 mm (5 to 10 mil). The contact between wires at intersections is modeled using general contact. Automatic time stepping without mass scaling was employed. Loading times are taken sufficiently long to avoid significant dynamic effects.

Computation time is dependent on problem size and hardware, especially the number of cores in case of an explicit solver. A typical computation, e.g., the cylinder crush of a Nitinol stent consisting of approximately 100k degrees of freedom, required approximately 6 h to solve on a system with an Intel(R) Xeon(R) CPU E5-2697 v4 at 2.30 GHz, 128 GB memory, using 9 cores. The loading for this problem was accomplished in 0.1 s simulation time with a stable time step of approximately 6.3E−8 s.

2.1.1. Model validation

Validation of the finite element beam model has been performed by comparing results of bench tests on a Wallstent with computational results, see Figs. 2 and 3. The investigated stent has a length of 60 mm, an outer diameter of 16 mm and is woven of 30 wires with a diameter of 6.5 mil at a pick rate of 10. The wires are manufactured from a biomedical grade cobalt-chromium-iron-nickel-molybdenum alloy (commonly known as Elgiloy or Conichrome) containing an enhanced radiopaque tantalum core.

Several tests were used: radial compression and release, plate crush and cylinder crush. In the radial compression test the diameter of the stent is first reduced from nominal to 4 mm by closing a metal iris (i.e., an adjustable diaphragm for regulating the size of a central hole). Subsequently, the diameter of the iris is increased, and the stent is allowed to regain its original diameter (Dabir et al., 2018). Friction between the iris and the stent is low and the stent can elongate during loading.

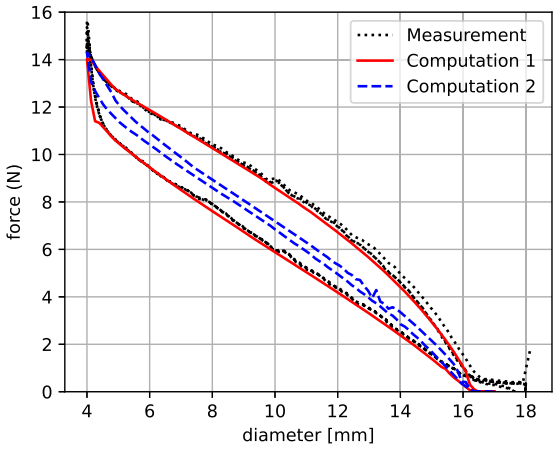

(a) Radial crimp force. Computations with different coefficients of friction between tool and stent, μ_t, and inter-wire, μ_w. Computation 1: $\mu_t = 0.15$ and $\mu_w = 0.10$, Computation 2: $\mu_t = 0.00$ and $\mu_w = 0.40$

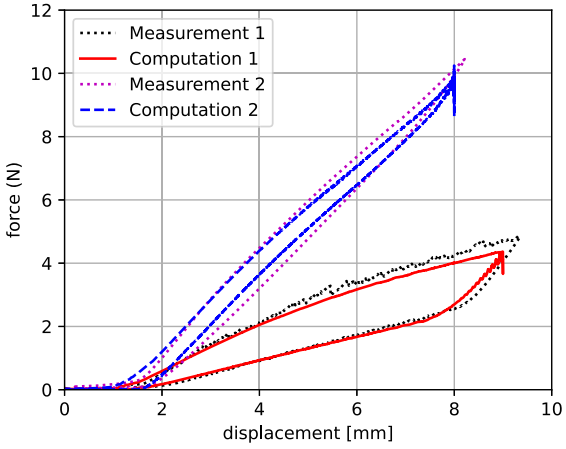

(b) Plate crush. Measurement 1 and Computation 1: crush between steel plates, friction coefficient between tool and stent $\mu_t = 0.10$. Measurement 2 and Computation 2: crush between silicone covered plates, $\mu_t = 1.50$.

Fig. 2. Braided stent model validation: Measured and computed force–displacement values.

A radial compression tester typically employs an iris consisting of 8 to 12 plates placed to construct a circular central hole. These plates are modeled as rigid elements of a cylinder. Reducing the diameter of this cylinder by displacing the nodes in radial direction effectively mimics the experimental radial compression tester. It was found that the number of plates did not have a significant effect on the mechanical response of the stent. Employing more plates clearly results in a more accurate description of the cylinder geometry and has a beneficial effect on the computations: the resulting deformation is smoother and force oscillations due to intermittent contact vanish. Therefore, 30 plates are used to model stent crimping.

In the plate crush test the entire stent is compressed between two plates up to 50%. The plates are covered by a layer of silicone, Shore A 20, to introduce friction, preventing the stents from accommodating the deformation through radial crimp. In the cylinder crush test, the stent is placed on a silicone covered plate after which a 10 mm diameter metal cylinder, with its axis perpendicular to the main axis of the stent, is used to compress the center region of the stent up to 50%. In the computational model, for both tests the silicone layers are approximated as rigid surfaces with adjusted friction. The frictional behavior of the stent on these surfaces is expected to be nonlinear with the apparent coefficient of friction increasing for higher normal forces as the wires are pushed into the silico surface thereby introducing mechanical interlocking. Within the scope of simulations in this section (i.e., to validate the global deformation behavior of the stent), the mechanical interaction between the stent struts and the silicone is effectively described by an apparent friction coefficient at macroscopic scale. Relevant local mechanisms such as mechanical interlocking are simply replaced by this macroscopic approach and fits the scope of these simulations. However, in Section 4, these mechanisms are included in more detail in the simulations.

The Young's modulus for the wires was determined by fitting the radial compression measurement data to the analytic solution for the pressure–diameter relationship for the woven metallic Wallstent as

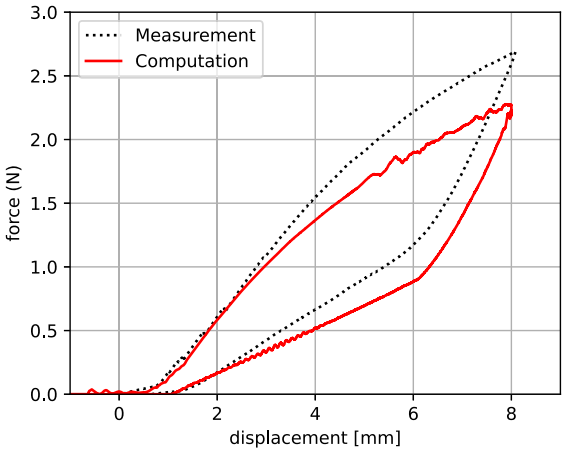

(c) Cylinder crush test result. Steel cylinder, friction with stent, $\mu_c = 0.10$, and silicone covered plate, friction with stent $\mu_t = 0.60$.

Fig. 2. (*continued*).

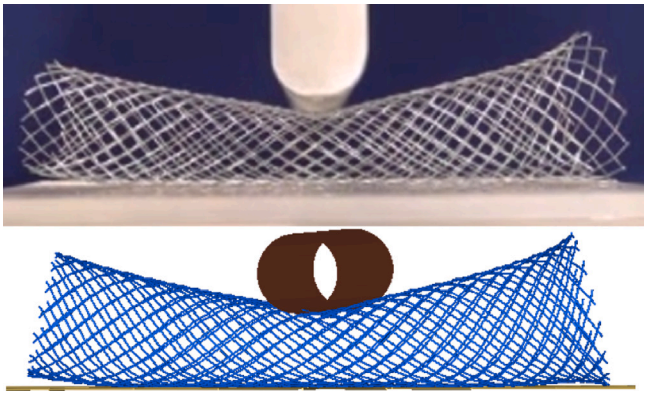

Fig. 3. Braided stent model validation: Measured and computed deformed geometry comparison. Cylinder crush, bench (top) and simulation (bottom).

Table 1
Parameters used for Nitinol (Clauwaert, 2012).

Parameter	Value	Unit
Austenite modulus	49074	MPa
Poisson's ratio	0.3	
Martensite modulus	20000	MPa
Poisson's ratio	0.3	
transformation strain	0.063	
AS start	143	MPa
AS finish	195	MPa
SA start	100	MPa
SA finish	30	MPa
AS compression start	280	MPa
Ref temp	310	K

derived by Wang and Ravi-Chandar (2004a). The obtained value is 210 GPa, which is in line with typical values for Elgiloy. The Poisson's ratio is set to 0.31.

Fig. 2(a) shows the measured force–diameter curve and two computationally obtained curves using different coefficients of friction (μ). By varying the friction coefficients, it was investigated whether the hysteresis is mostly due to friction between the stent and the tool rather than due to wire to wire friction. For Computation 1, the friction coefficient between the stent and the tool $\mu_t = 0.15$ and the inter-wire friction coefficient $\mu_w = 0.10$, while for Computation 2 the inter-wire friction coefficient $\mu_w = 0.40$ while the stent to tool contact is frictionless. The first simulation shows a good agreement with the measurement, exhibiting a similar amount of hysteresis, while the latter exhibits too little hysteresis, indicating that wire to wire friction does not play a significant role. For the subsequent computations, the inter-wire friction coefficient is set to $\mu_w = 0.10$. Note that especially in the case of radial compression the symmetric loading results in very little sliding of the wires over each other, but instead, the wires rotate relative to each other around the crossover points. This rotation is also the underlying cause of the observed increased stiffness when approaching a diameter of 4 mm. At these smaller diameter values the wires, due to their weaved pattern, start obstructing their relative rotation and the wires are forced to bend in the radial plane to accommodate the prescribed diameter decrease. At this stage also an increase in hysteresis due to inter-wire friction can be observed as wires are forced to slide over one another.

In Fig. 2(b) measurements and computational results of plate crush tests are depicted. Two variants of this test have been performed, one with the stent between steel plates and another where a silicone layer is placed on top of the steel plates. Upon loading, the wires of the stent are pushed into the soft silicone leading to mechanical interlocking and increasing the apparent friction between the stent and the plates, restricting the movement of the wires and increasing the crush resistance. The μ values used for the computations are determined by fitting the force–displacement curves. For the test with silicone covered plates a good agreement is achieved with a μ_t of 1.50, both for the force levels as well as the hysteresis. For the test using steel plates a good agreement is found between the computations and the measurement with a friction coefficient, μ_t, of 0.20 for the contact between stent and plates. Note that in this case, μ_t is higher than in the radial compression test, which may be explained by the difference of material and surface roughness of the radial compression tester and the metal plates used for the plate crush.

Fig. 2(c) shows the results for the measurement and computation of the cylinder compression tests, a metal cylinder and a silicone covered plate are used. Here, the amount of hysteresis matches well for a μ_t of 0.60. It can be observed that the resistance force is being underestimated for larger cylinder displacements. This may be attributed to the simplified model of the silicone layer that does not accurately describe mechanical interlocking.In the case of this cylinder crush the mechanical locking will be high directly under the compressing cylinder, while towards the stent ends it will gradually diminish. This is why the effective friction coefficient for this test is lower than for the plate crush test.

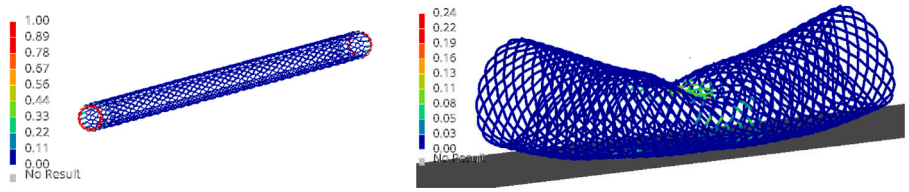

(a) Stent subjected to radial crimp. (b) Stent subjected to cylinder crush.

Fig. 4. Martensite volume fraction in deformed Nitinol stents. The maximum value in the cross section is shown.

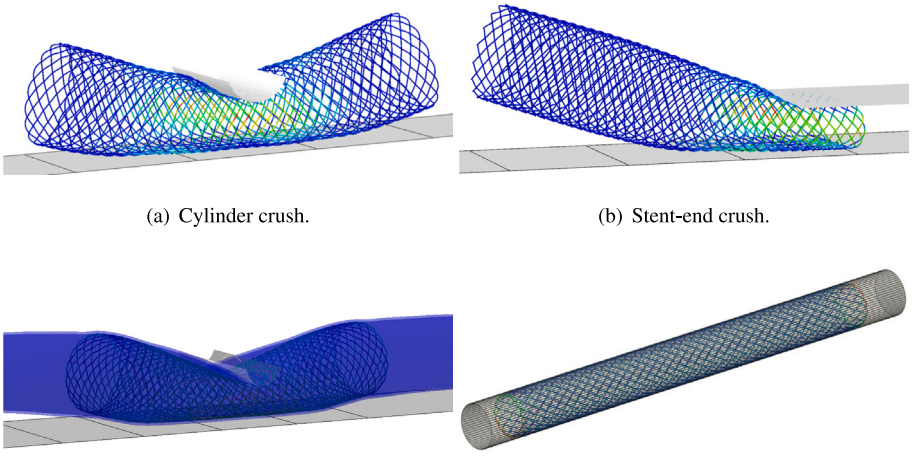

(a) Cylinder crush. (b) Stent-end crush.

(c) In-vein cylinder crush. (d) Uniform radial compression.

Fig. 5. Characterization tests for the braided stent. The colors indicate strain levels.

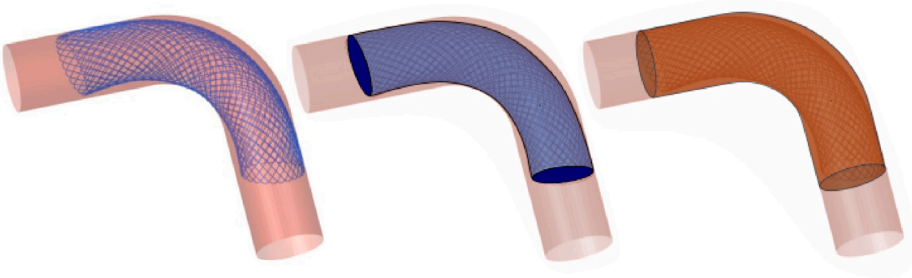

Fig. 6. Conformability is defined as the ratio between the stent volume (blue, center) and tube volume (red, right).

The validation of the finite element model is performed on the Wallstent made from Elgiloy, however, the braided stents investigated in this work are made from Nitinol. The focus lies here on the effect of design parameters on the stent performance, while the material properties are kept constant. The parameters used for the braided Nitinol stents are taken from Clauwaert (2012) and are given in Table 1. For all calculations the temperature is assumed to be constant at 37°C (310 K). The inter-wire friction coefficient, μ_w, for Nitinol is set to 0.10, equal to that used for the Elgiloy wires. For contact between stent and silicone covered plates a friction coefficient, μ_t, of 0.90 is taken, while for contact between the stent and metallic surfaces a coefficient of 0.20 is assumed.

Since the stents being investigated in the remainder of the manuscript are made of Nitinol, the phase transitions of the material may affect the force levels and energy dissipation. Even though this typically is very much the case for laser cut stents, braided Nitinol stents deform mostly elastically. This is shown in Fig. 4, where the maximum volume fraction of martensite is depicted. In the case of radial crimp, full transformation was reached but only locally in the looped ends of the stent. For the stent subjected to cylinder crushing locally only up to 25% transformation is reached.

2.2. Laser cut stent model

For benchmarking reasons two laser cut stents have also been included in the study. Their geometries are taken from the commercially available Abre™ and Venovo™ stents using micro-CT imaging. Since the interest here is in geometric design features, the material properties are taken equal to those of the braided stents. For these types of stents a 1D beam approach is not suitable because of inhomogeneous cross sections and oversimplified description of the geometry where beams meet under small angles and where consequently stress inhomogeneities are expected. The element type used for the stent with the explicit solver developed by Altair, Radioss, is C3D8I. A mesh convergence study was performed to determine the required element size, in cross section, 3 by 3 hexagonal elements were found to be sufficient. Mass scaling was applied to increase the time step by a factor of 10. The validity of mass scaling was checked though analysis of a radial compression test of the

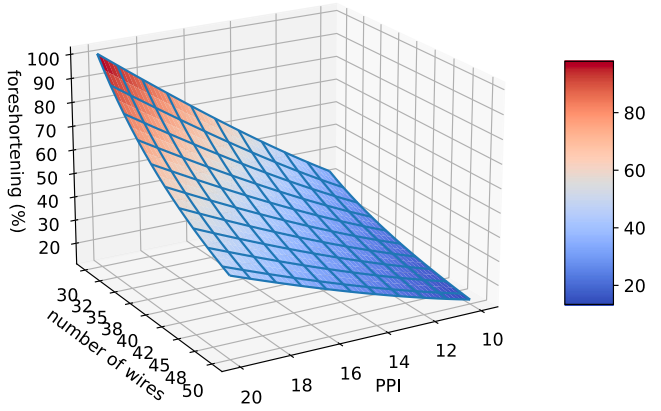

Fig. 7. Foreshortening percentage of a 16 mm diameter braided stent deployed in a 12 mm diameter rigid vessel, from Eq. (1).

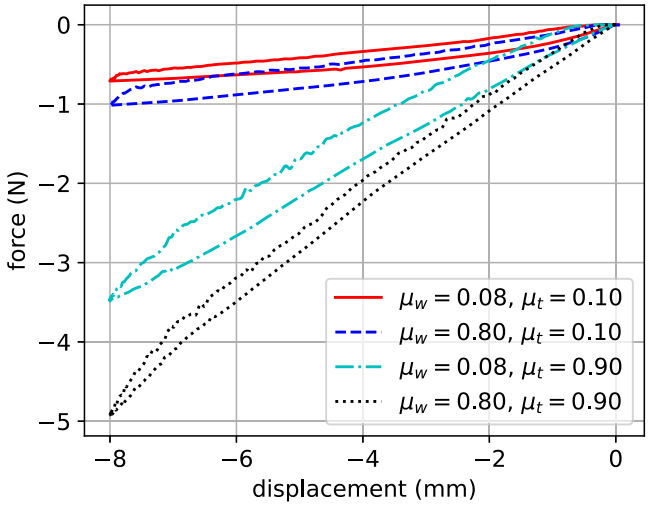

Fig. 8. Effect of friction coefficient between the wires, μ_w, and between the wires and the test equipment, μ_t, on the force displacement curves.

Abre stent from diameter 16.3 mm to 10 mm in 0.05 s. The stable time step without mass scaling is approximately 1E-8 s. Mass scaling to 1E-7 s exhibited a low enough kinetic to internal energy ratio, less than 0.05, over the majority of the loading case.

3. Stent performance characterization tests

The main function of venous stents is to ensure patency, not only by increasing the lumen of a stenotic vessel by applying a chronic (radial) outward force, but also by preventing external loads from crushing the vein which is the case for the May–Thurner syndrome. This mechanical support should be provided in an environment that can be tortuous, non-homogeneous and movable. Beside the functional characteristics to the stent additional requirements relate to its deployment process; navigation to the lesion site and accurate positional deployment. Based on performance parameters for venous stents – foreshortening, chronic outward force, resistance to localized crushing, conformability – specific tests have been selected and suitable metrics defined.

Crush resistance is evaluated using three different tests: Two cylinder crush tests resembling May–Thurner syndrome type loading where the load is centrally placed, Figs. 5(a) and 5(c), and a test to assess the crush resistance of the ends of the stent, see Fig. 5(b). For the latter the outer 10 mm of a stent lying on a plate is compressed with a second plate. In all cases, computations are performed to calculate the required force for compression up to 50% of the stent's nominal diameter.

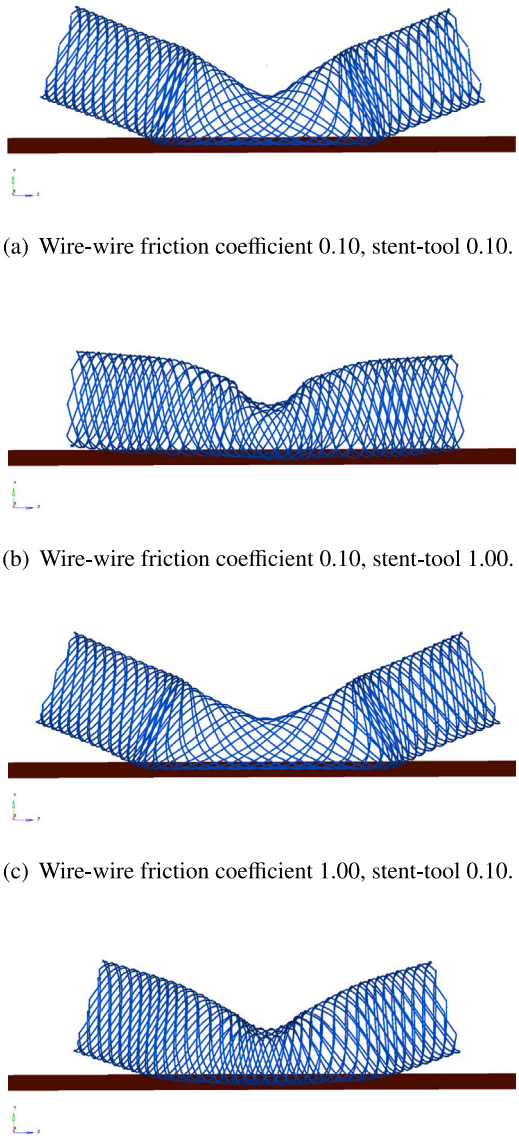

(a) Wire-wire friction coefficient 0.10, stent-tool 0.10.

(b) Wire-wire friction coefficient 0.10, stent-tool 1.00.

(c) Wire-wire friction coefficient 1.00, stent-tool 0.10.

(d) Wire-wire friction coefficient 1.00, stent-tool 1.00.

Fig. 9. Influence of coefficient of friction on deformation of an open-ended braided stent compressed by a cylinder: maximum principal stress in the deformed configuration.

For the May–Thurner type tests, the stents are crushed between a 10 mm diameter cylinder and a bottom plate, both assumed rigid. In the first case, Fig. 5(a), denoted as cylinder crush, the stent is placed unconstrained on the bottom plate and in the second case, Fig. 5(c), cylinder crush in-vein the stent is deployed in a vein by first radially crimping the stent, then placing the crimped stent in the vein, followed by radial expansion whereby the stent comes into contact with the vein. The deployment of the stents is therefore not modeled as clinically achieved, by gradually removing the delivery catheter from the stent, but rather by allowing the stents diameter to increase homogeneously over its entire length. This approach results in the most optimal final positioning of the stent. The artificial vein is modeled as a silicone tube, using a hyperelastic Mooney–Rivlin material (Shore A 30: C_{10} = 97.5 kPa, C_{01} = 24.4 kPa, D_1 = 1000 1/kPa) with a wall thickness of 0.46 mm, representative of an iliac vein Brass and Kassab (2019). For this specific test, the diameter of the vein is set to 1 mm smaller than the nominal diameter of the stent.

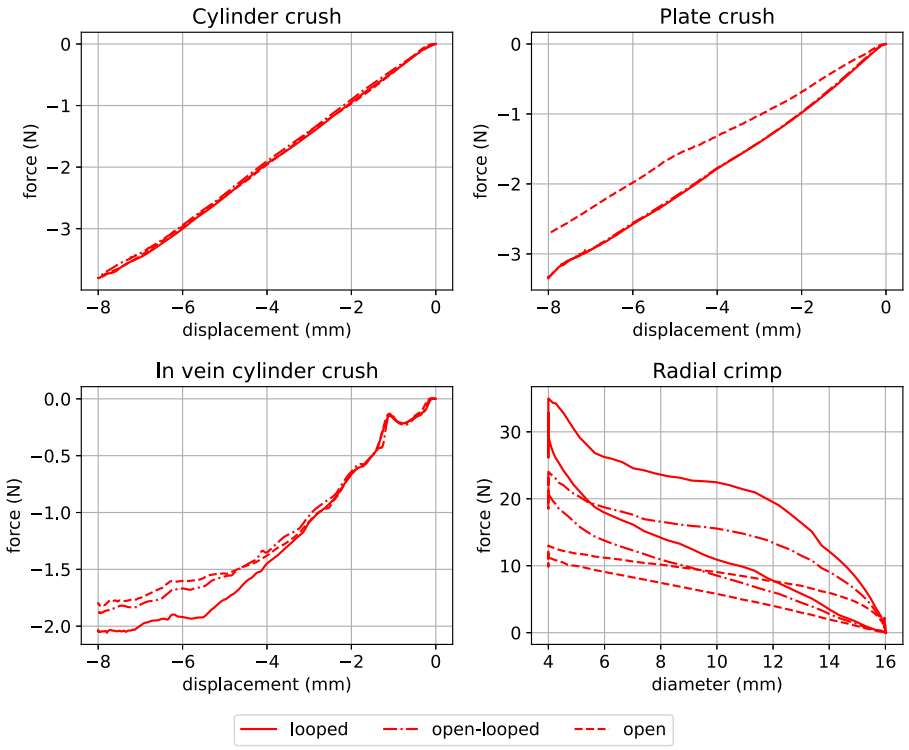

Fig. 10. Characterization tests for stents with different end types.

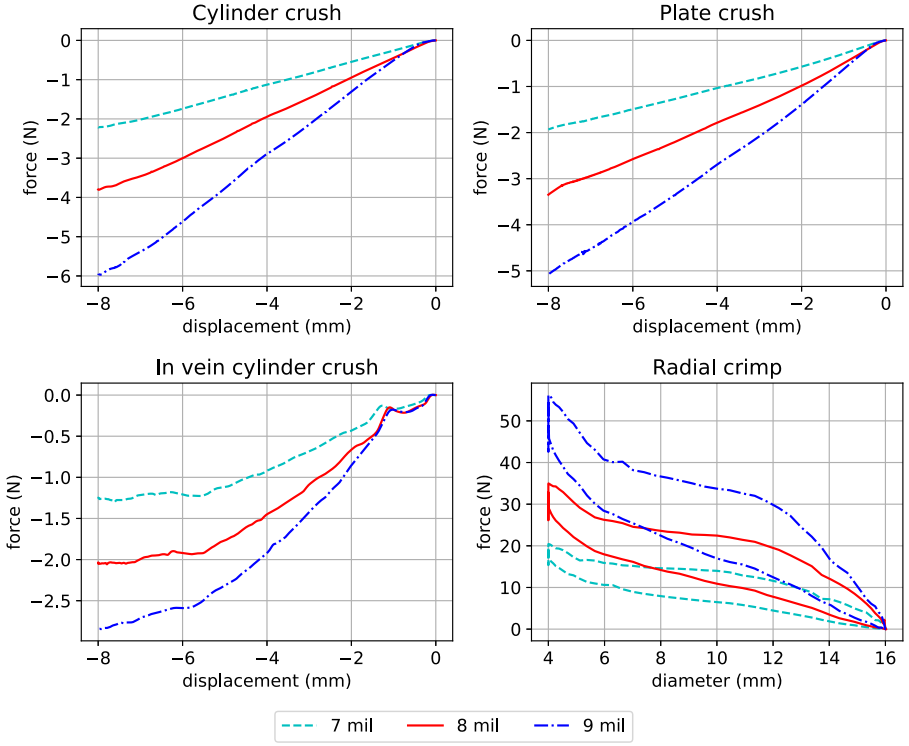

Fig. 11. Characterization tests for stents with different wire diameters.

Chronic outward force is assessed based on the force exerted by the stent on a tube after first radially compressing the stent using a rigid cylinder, as described in Section 2.1.1, to 4 mm diameter followed by releasing to 80% of the stent's nominal diameter, see Fig. 5(d). For this test, the complete load path needs to be accounted for since the stent consists of a shape memory alloy whose response is history dependent; During radial compression some of the material undergoes phase transformation from austenite to martensite and consequently its stiffness is reduced. Since the phase transitions occur at different stress levels during loading and unloading the state of the material at 80% diameter is different when having been compressed to smaller diameter first, more material will be in a martensite phase compared to a single

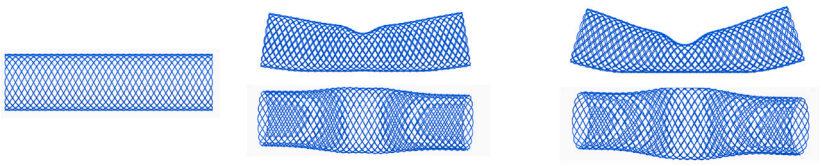

(a) Stent with 32 wires.

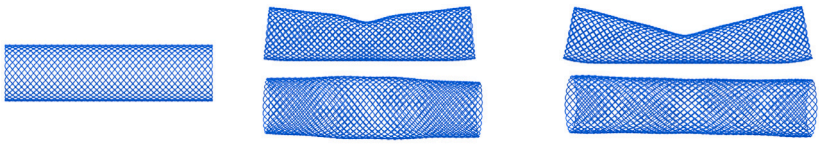

(b) Stent with 48 wires.

Fig. 12. Deformed geometries (top and side views) of a 32 wire and a 48 wire stent subjected to cylinder crush. From left to right, geometries are shown at 0%, 30% and 50% nominal diameter compression.

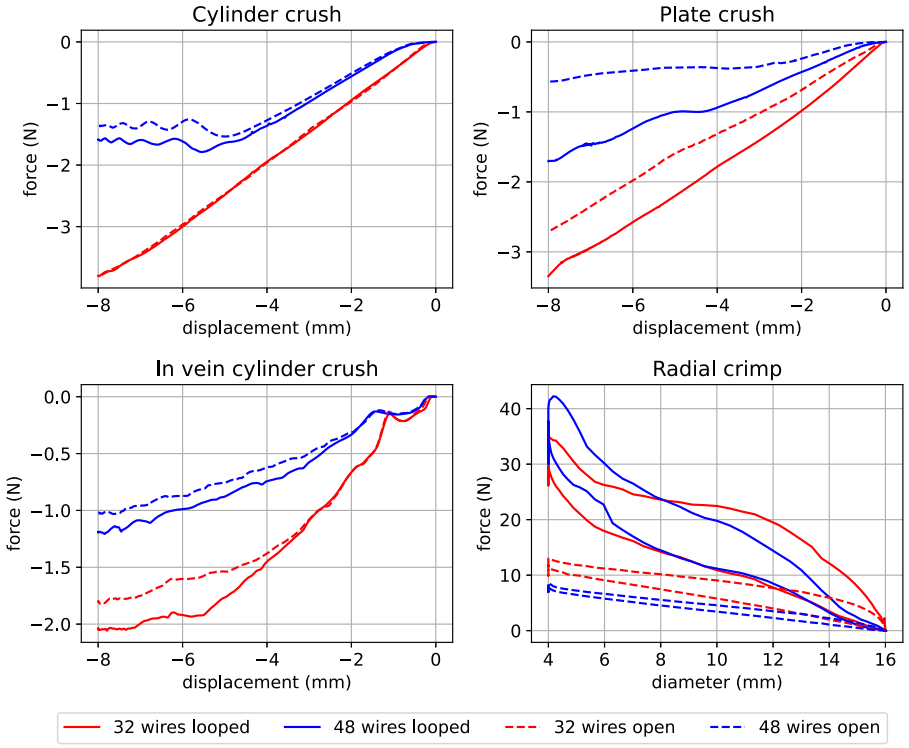

Fig. 13. Characterization tests for stents with different wire amounts.

compression step from 100% to 80% and hence the stent will have a lower chronic outward force. For the unconstrained compression tests this preconditioning step is not required as all the material will have been reverted to austenite once the stent has been allowed to return to its original diameter.

Conformability is investigated by deploying stents in a bent tube, 15 mm diameter, 90 degrees, 20 mm radius, and assessing wall apposition. Apposition is quantified by the ratio of the volume occupied by the lumen of the stent and the lumen volume of the tube occupied by the stent, see Fig. 6.

Foreshortening is evaluated based on the stent length increase after radial compression into 10 Fr catheter with 2.9 mm inner diameter, the typical catheter size for this type of stent.

Table 2
Parameter ranges, nominal values in bold.

Feature	Symbol	Unit	Values
wire diameter	d	mil (1/1000 inch)	7,**8**,9
pick rate	P	1/inch	12,**15**,18
number of wires	N	–	**32**,48
end design/type	–	–	**LL**, LO, OO
stent length	L	mm	40, **60**, 120

4. Results

The nominal configuration of the braided stent is 8 mil diameter wire, 16 mm outer diameter, 60 mm length, 15 ppi, 32 wires and both ends looped, as indicated by the bold values in Table 2.

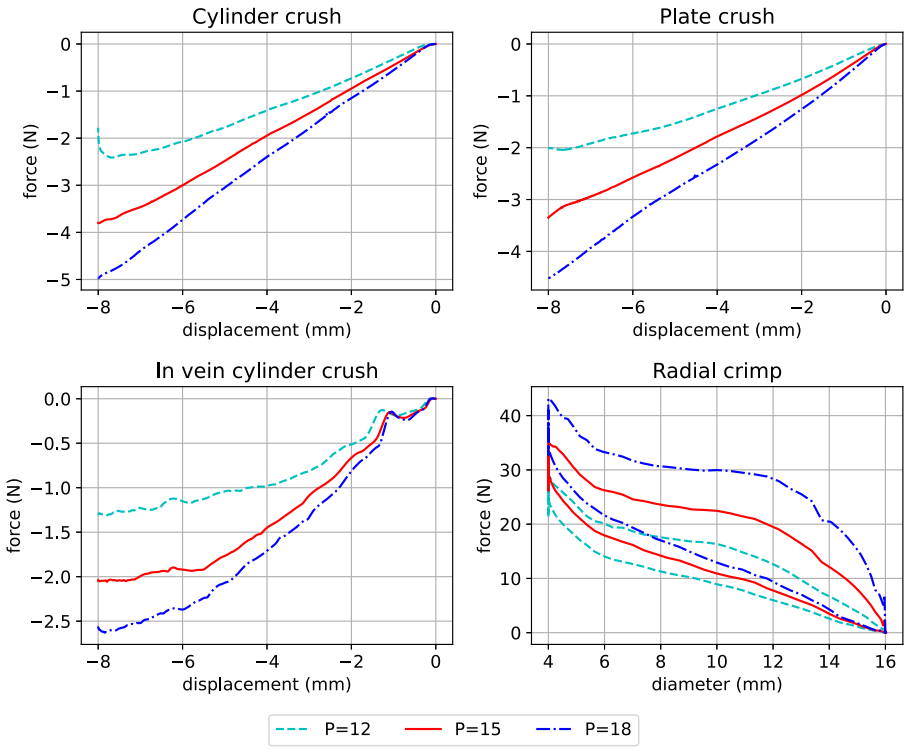

Fig. 14. Characterization tests for stents with different pick rates.

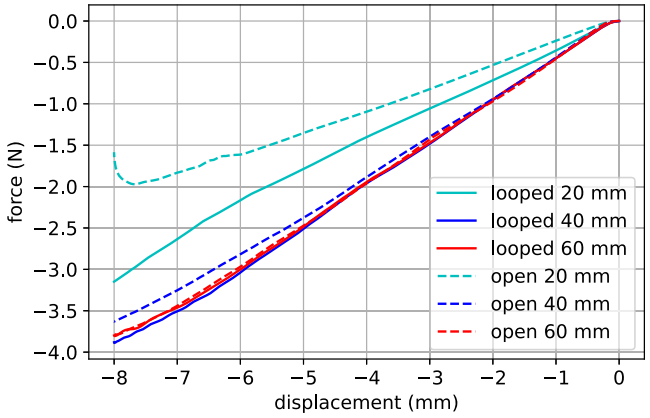

Fig. 15. Force–displacement curves for open and looped end stents with various lengths under cylinder compression.

4.1. Foreshortening

Based on geometrical considerations an analytical equation can be derived for the foreshortening of a braided stent:

$$\frac{\Delta L}{L_0} = \frac{L_s(D) - L_s(D_0)}{L_s(D_0)} = \sqrt{\left(\frac{2\pi P_0}{25.4N}\right)^2 \left(D_0^2 - D^2\right) + 1} - 1 \tag{1}$$

with D_0 the nominal or initial and D the diameter of the stent when deployed. The assumption is that the ends are open and radial movement is accomplished by only torsion of the wires. Also, fish mouthing, which occurs when radially compressing a stent, is not accounted for in the derivation and will slightly reduce the amount of foreshortening. Through comparing with computational radial compression results it has been confirmed that the equation is also valid for closed loop stents, as also shown in Shanahan et al. (2017a). Foreshortening as a function of pick rate and number of wires is plotted in Fig. 7. The figure shows the relative elongation of a 16 mm diameter stent when deployed in a 12 mm rigid tube. It can be observed that the amount of foreshortening increases with decreasing number of wires and increasing pick rate.

4.2. Friction

To further investigate the effect of friction on the behavior of braided stents, computations of cylinder crush experiments are performed with varying friction coefficients for the interaction between wires (0.10 and 0.80) and between wire and bottom plate (0.10 and 0.90). Figs. 8 and 9 show the resulting force versus displacement curves and deformed geometries, respectively.

The reaction force depends on both the friction between the wires and between the wires and the testing device. However, the latter has a much stronger influence. The hysteresis observed in the tests finds its origin in both friction sources as well, increasing with higher coefficients of friction. However, friction also has a significant effect on the deformation behavior of the stent, see Fig. 9. With low friction between the test equipment and the stent, the wires may slip during compression, effectively increasing the pitch angle and thereby decreasing the PPI, and thus weakening the crush resistance, see Figs. 9(a) and 9(c). Note that in this manner different deformation mechanisms of the stent are being triggered, giving rise to different stress distributions and crush resistance levels. Without sufficient friction a braided stent can accommodate a load by rotating wires relative to each other and low levels of torque in the wires, which presents only very little resistance, while high stent to environment friction levels effectively restrict axial movement of the stent and hence the wire rotations, forcing the wires to bend resulting in higher levels of resistance.

A higher wire-to-wire friction inhibits relative movement between the wires and causes the stent to bend around the compressing cylinder, see Figs. 9(b) and 9(d).

4.3. Stent end type

Three configurations of stent end types have been investigated: (i) both ends open, similar to the wall stent, (ii) one side looped, and

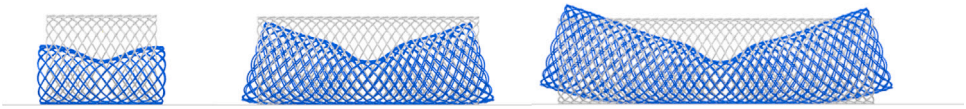

(a) Looped, 20, 40 and 60 mm.

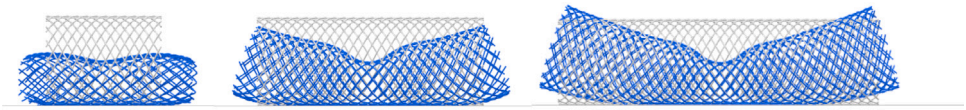

(b) Open, 20, 40 and 60 mm.

Fig. 16. Initial and deformed geometries of short stents under cylinder compression.

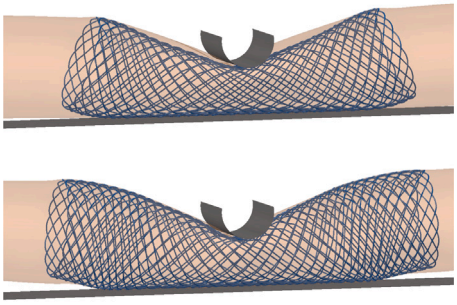

(a) Deformed geometries 40 mm (top) and 60 mm stent (bottom).

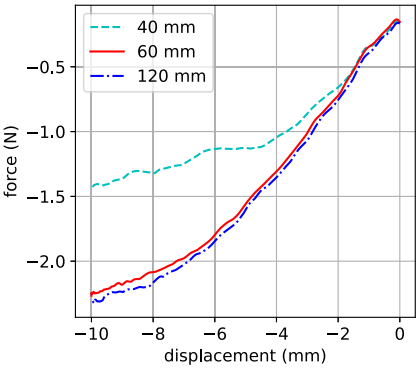

(b) Force-displacement curves.

Fig. 17. In-vein cylinder compression tests on looped stents with varying lengths.

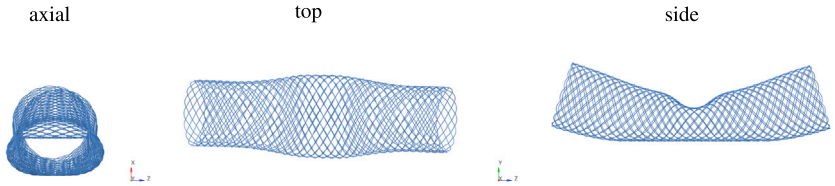

(a) Looped cylinder crush.

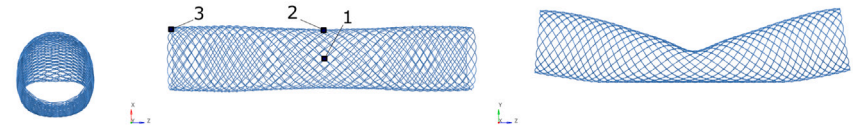

(b) Looped cylinder crush in-vein.

Fig. 18. Deformed stent geometries after cylinder crush and cylinder crush in-vein tests, from left to right: front, top and side views.

(iii) both ends looped. Fig. 10 shows the effect of the end type on the characterization test result. It can be observed that the end type does not affect the crush resistance of the cylinder crush test since the deformation is localized in the center of the stents, sufficiently far away from the ends to avoid their influence. In the cylinder crush in-vein test the looped ends cause an increase in crush resistance for larger cylinder displacements. Here, the looped ends prevent the stent from fish mouthing, resulting in better wall apposition and consequently more frictional resistance. The plate crush test shows an increased resistance provided by a looped end. Additionally, from the test on the stent with a single side looped, it is clear that the distal open end does not affect the resistance since the result is identical to that of a stent with both ends looped. The radial compression test shows markedly different results for every type, with the looped ends increasing not only the resistance significantly, but also the hysteresis as a result of friction.

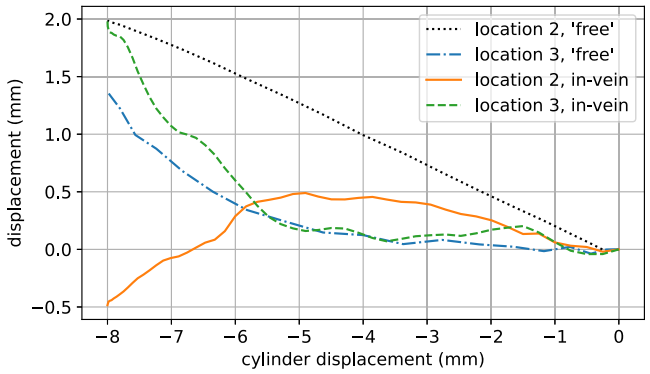

Fig. 19. Displacement of key locations, see Fig. 18, on stent during cylinder crush test.

4.4. Wire diameter

The effect of wire diameter on the characterization tests is shown in Fig. 11. One of the main deformation mechanisms is bending of beams, thus the force depends on the second moment of area, i.e., the wire diameter to the fourth power, d^4. This dependence can be observed in all tests on free stents, which can be mapped onto each other by scaling with d^4. The cylinder crush in-vein test shows a different relation as the vessel to stent interaction introduces more complex behavior.

4.5. Number of wires

Fig. 13 shows the results for open and looped stents with 32 and 48 wires. The pick rate is kept constant which means that the pitch angle effectively increases with an increasing number of wires. For the cylinder crush of the free stent no significant difference is observed between the open and looped stents. The high wire count stents have a lower crush resistance and are more prone to slip of the wires over the plate resulting in a plateauing of the force curve.

When keeping the pick rate constant, the higher wire count results in an increase of the winding angle, i.e., the wires become more aligned with the axial direction of the stent. Cylinder crushing results in axial elongation of the stent and radial reduction through a wire rotation mechanism, which is typical for braided stents. To illustrate this, Fig. 12 shows the deformation of stents with 32 and 48 wires and subjected to cylinder crushing. For the 32 wires stent, Fig. 12(a), this leads to a local deformation in the vicinity of the compressing cylinder, as is visible in the side view, and a significant broadening of the stent, visible in the top view for 30% and 50% compression. In contrast, the 48 wires stent, Fig. 12(b), shows a similar behavior up to 30% compression, after which the deformation mechanism at 50% compression changes to a radial reduction through axial expansion which can be observed in the top view as a narrowing of the stent directly below the compressing cylinder. Clearly, these deformation mechanisms are dependent on the potential interaction mechanisms of the stent (e.g., caused by surrounding tissue) as these govern the axial extension of the stent.

A similar behavior is seen for the cylinder crush in-vein test where the force curves start deflecting down when the stents start slipping inside the vessel. The looped stents start slipping later than the open ones indicating that their frictional forces are higher, which is in line with their higher radial outward forces. It is also observed that the hysteresis is higher for stents with lower wire counts. This can be explained by the smaller pitch angle which results in more axial elongation of the stent for equal radial compression, and consequently more dissipation due to friction.

4.6. Pick rate

The pick rate, P, is one of the parameters that controls the pitch angle, α, together with the diameter of the stent D, and the number of wires, N:

$$\alpha = \arctan\left(\frac{25.4N}{2\pi DP}\right). \tag{2}$$

Increasing the pick rate while keeping the number of wires constant, i.e., reducing the pitch angle, increases the amount of material and stiffens the stent for all types of loading, see Fig. 14. Conversely, increasing the number of wires while keeping the pick rate constant results in a smaller pitch angle and lower crush resistances, see Fig. 13. Note that for the stent with pick rate 12 the force curve of the cylinder compression test exhibits a drop when approaching 8 mm. This is the result of the stent changing the deformation mechanism from local deflection and broadening to axial extension and radial reduction.

4.7. Stent length

Cylinder crush tests have been computed for open and looped stents with length values 20, 40 and 60 mm. The resulting force–displacement curves are depicted in Fig. 15. The looped stents of 60 and 40 mm and the open 60 mm stent exhibit similar crush resistance, the 20 mm open and 40 mm, stents show a lowered resistance, with the open-ended stent giving the lowest resistance. It appears that the observed differences are the result of an edge effect. When the load is placed sufficiently far from the edge of the stent, the edge does not affect its response, as evidenced by the similar curves for the 60 mm open and looped stents in Fig. 15 and the similar shapes of the deformed stents in Fig. 16. For sufficiently long stents the ends do not deform, while for progressively shorter stents the ends start to compress, clearly visible for the 20 mm stents. The effect is more pronounced for open stents where for short enough stents fish mouthing starts to occur. The deviation in the force of the 20 mm open-ended stent in Fig. 15 is the result of slip between the plate and the stent allowing the axial extension-radial reduction mechanism. This does not yet occur for the 20 mm looped stent since its resistance to axial extension is not only determined by friction with the tool, but also by the looped ends which would need to bend locally to allow the extension. This effect is stronger closer to the ends; hence it is most noticeable for the shorter 20 mm stent.

An edge effect is also observed for the cylinder crush in-vein test, see Fig. 17, which shows the deformed geometries for stents of 40 and 60 mm length with a diameter of 20 mm and the force–displacement curves. From the curves it may be observed that the edge effect disappears as the stent becomes longer; the 60 mm long stent (3 times the diameter) shows an almost identical response to the 120 mm stent (6 times the diameter). However, the 40 mm stent (2 times the diameter) shows a much lower crush resistance compared to the two longer stents. From Fig. 17(a) it may be observed that the 40 mm stent deformed differently from the 60 mm stent, elongating more and effectively increasing the pitch angle (reducing the pick rate) resulting in a lower resistance. The interaction between the ends of the 60 mm stent and the vein prevent the stent from elongating, maintaining a lower pitch angle overall. A gradient of the pitch angle is observed in this case with a decreased angle at the ends and an increased one in the middle of the stent.

4.8. Cylinder compression: free vs in-vein stent

Deployment of a stent in a vessel changes the boundary conditions and consequently the mechanical behavior significantly. Fig. 18 shows the deformed configurations of stents subjected to the cylinder crush and the cylinder crush in-vein tests. In this figure key locations on the stent are indicated; location 1 is positioned directly under the

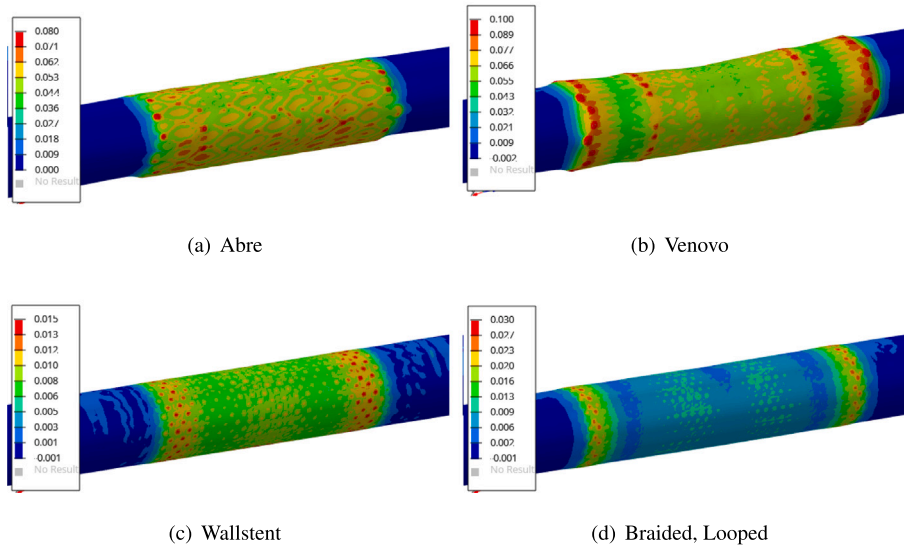

(a) Abre (b) Venovo

(c) Wallstent (d) Braided, Looped

Fig. 20. Stresses in the vessel wall after stent deployment.

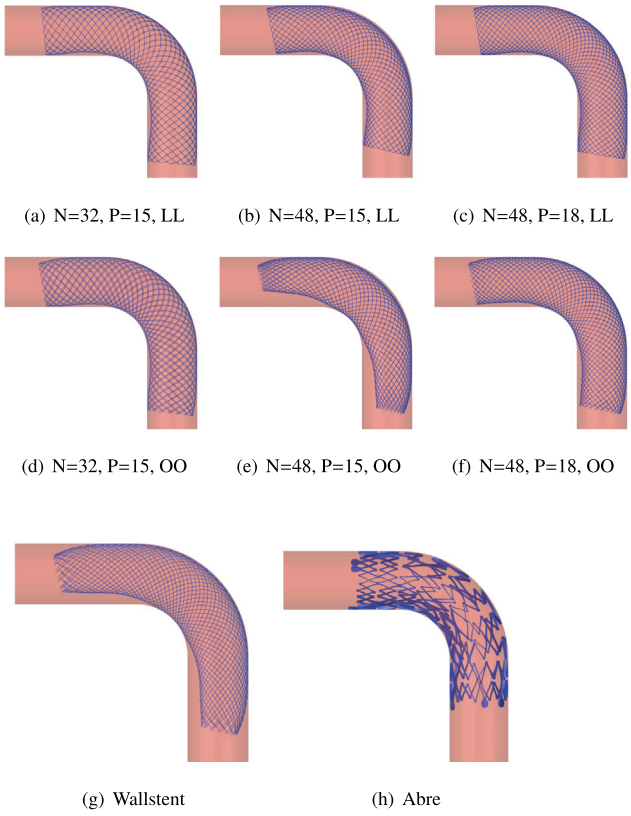

(a) N=32, P=15, LL (b) N=48, P=15, LL (c) N=48, P=18, LL

(d) N=32, P=15, OO (e) N=48, P=15, OO (f) N=48, P=18, OO

(g) Wallstent (h) Abre

Fig. 21. Conformability study of stents in a 90 degree bent tube.

compressing cylinder in the center of the stent and will move downward, location 2 is also under the compressing cylinder but on the side of the stent, this location will move downward and laterally, and finally location 3 is placed at the end of the stent, where it will move predominantly in axial direction.

When the stent is not restricted by a vessel, it will respond to the load by expanding laterally under the cylinder. Contrarily, when loading a braided stent deployed inside a vessel, the segment under the cylinder crimps radially and becomes narrower compared to the outer segments of the stent. The deformation history of the stent in the latter case consists of two phases, as can be observed in Fig. 19.

Fig. 19 shows the displacement of locations 2, in lateral direction, and 3, in axial direction, versus the vertical displacement of location 1 for both the cylinder crush and cylinder crush in-vein cases. For the cylinder crush where the stent is not obstructed by a vessel, as the cylinder moves down, compressing the stent, location 2 moves monotonously outward while the stent lengthens, indicated by the displacement of location 3. For the cylinder crush in-vein however, initially, location 2 moves outward, but changes direction when the stent starts sliding inside the vein, indicated by an increased axial movement of location 3 in this test after approximately 5.5 mm compression. The sliding also coincides with a decrease in the crush resistance stiffness as visible in Fig. 10 by the changing slope of the load displacement curves.

4.9. Device-tissue interaction

Deploying a stent in a vessel with a smaller diameter than the nominal (unloaded) stent diameter, i.e., oversizing, results in a chronic outward force exerted by the stent. The magnitude of this force may differ considerably between stents, see Dabir et al. (2018). Additionally, the force is not distributed homogeneously over the tissue.

Computations have been performed, deploying 16 mm diameter stents in a 15 mm diameter vein analogue. The vessel analogue is modeled as a hyper-elastic material, see Section 3. Fig. 20 shows the resulting stresses in the vessel wall. Note that the colorbars differ between the stents to visualize the distributions. The mechanical description of the vessel analogue is a simplification of actual vein behavior, however, trends observed in these simulations still allow for an assessment of stent performance in actual physiological conditions.

The braided stents yield significantly lower stress levels in the tissue compared to the laser cut stents. Between the braided stents the open-ended stents provide a more homogeneous stress field over their length, while the looped stents concentrate more of the radial outward force at the ends. The higher outward forces produced by the laser cut stents also lead to noticeable bulging of the vessel, which is especially apparent for the Venovo stent with its flared ends in the unloaded configuration. After deployment in the vessel this leads to stress concentrations at the ends. Geometric features likes this will have a positive effect on preventing stent migration, however, they may also lead to disturbance of the flow by changing the local curvature at the entrance and exit of the stent and promote in-stent restenosis (Gijsen

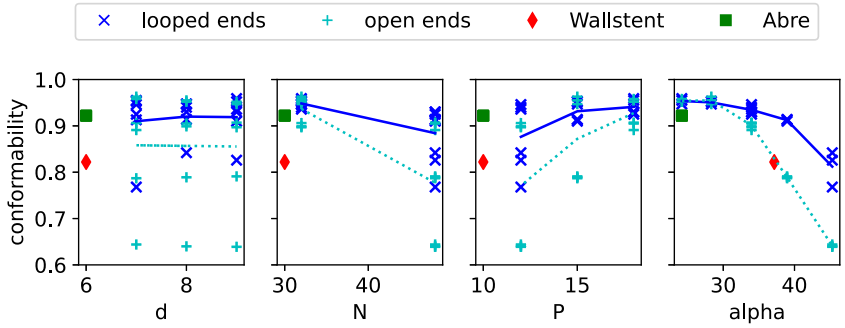

Fig. 22. Main effects plot for conformability.

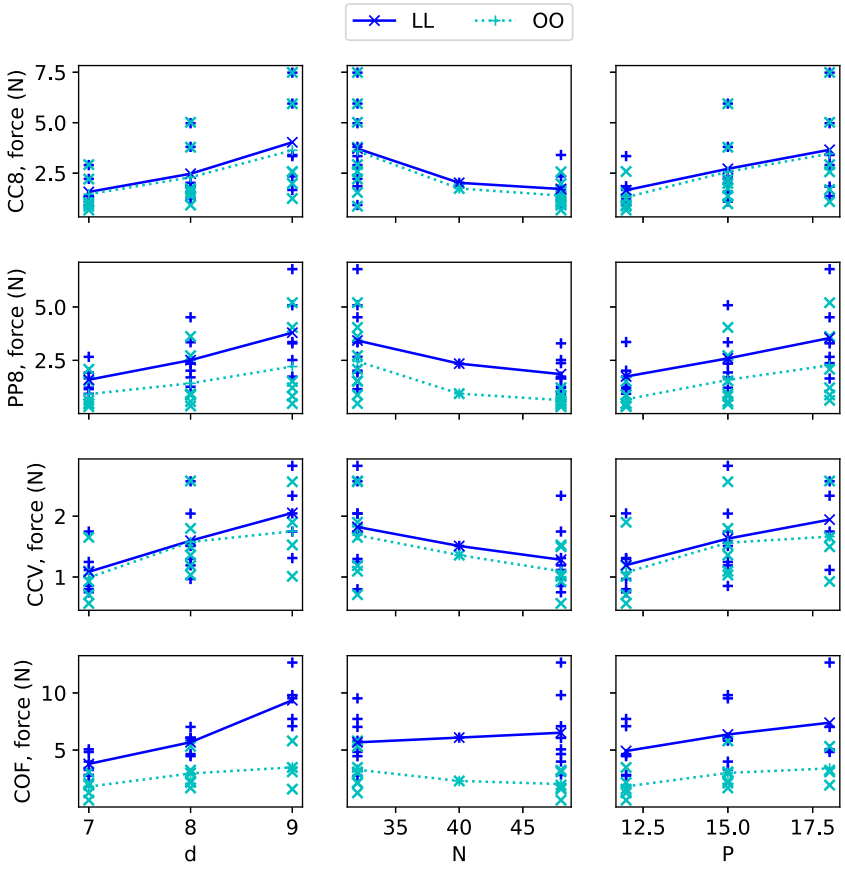

Fig. 23. Main effects plots. CC: cylinder crush resistance force, PP: plate compression resistance force, CCV: crush resistance in-vein, COF: chronic outward force at 80% nominal diameter, d: wire diameter, N: the number of wires, P: pick rate.

et al., 2019). In addition to flow factors, mechanical induced stresses may also stimulate in-stent restenosis (Jenei et al., 2016; Lally et al., 2005). Stent selection is therefore a trade-off between the amount of stent oversizing to optimize patency and avoid stent migration, while keeping the mechanical load on the vessel wall and the disturbance of the flow within limits is therefore essential.

4.10. Conformability

Deploying the braided stent in a curved tube may lead to poor apposition, i.e., the stent is not able to deform sufficiently to follow the curvature of the tube, see Fig. 21. For the open-ended stents, including the Wallstent, this may result in severe fish mouthing. The Abre stent is shown to have very good apposition, as its structure of circular segments, which are connected on three radially positioned points, allows each segment to almost conform to the local tube direction independently.

Fig. 22 shows the main effects plots for conformability (ratio of volumes encompassed by stent and stented region of the vessel, Section 3) with respect to the wire diameter, wire amount and pick rate. Overall, the looped stents perform better than the open-ended stents due to their resistance to fish mouthing. Looped and open-ended stents are both insensitive to the wire diameter but are sensitive to the wire amount and pick rate, with a negative correlation to the first and a positive correlation to the latter. From the relation of these parameters to the pitch angle, Eq. (2), and observations from Fig. 21, it follows that smaller angles allow the stent to follow curvature better, leading to improved wall apposition. In the graph showing conformability versus pitch angle in Fig. 22 the data points, per stent type, are grouped very closely together an indication the pitch angle is a critical feature when it comes to conformability. The result of the Wallstent aligns very well with those of the open-ended Nitinol stents. For lower pitch angles the open-ended and looped stents have equally good behavior, however,

as the pitch angle increases above 30 degrees the performance of the open-ended stents starts to drop, where the looped stents maintain conformability up to 40 degrees.

4.11. Main effects

Based on the data from the computations main effects plots are created for the wire diameter, number of wires and pick rate, see Fig. 23. The wire diameter and pick rate are observed to have a positive correlation with all responses. The number of wires shows a negative correlation for the crush resistance tests, but the chronic outward force appears insensitive to it in case of looped ends, while it does show a negative correlation for open-ended stents.

5. Discussion and conclusion

Finite element analysis was employed to analyze the effect of design parameters and device-tissue interaction on the performance of braided venous stents. A model was developed and validated consisting of numerically efficient beam elements where the interaction between the wires was accounted for properly through a contact algorithm, such that unphysical behavior that may arise from simplified approaches was avoided.

Several tests were proposed to evaluate the performance of the stents, aimed at quantifying their ability to provide patency and conformability. Computations with varying design parameters were performed and analyses of the results were presented that may be used as design guidelines.

The presented results illustrate that braided stents perform differently depending on interaction mechanisms, such as stent-tool friction, inter-wire friction and device-tissue mechanics. If the stent is free to expand or retract axially, it accommodates its new geometry by having wires rotate relative to each other and only small amounts of strain are required. However, when axial displacement is restricted, the behavior is much stiffer as the wires are forced to bend leading to higher levels of strain. It is shown above that the interaction between the stent and its surroundings has a significant impact on its behavior, specifically the difference between an unconstrained stent subjected to a cylinder crush test compared to a stent deployed in an elastic vessel subjected to this loading was shown to lead to significantly different results. Therefore, when designing a stent, it is essential to take the device-tissue interaction mechanisms into account.

After placement of a stent, reendothelialization may occur and the struts will be covered with a neointimal tissue layer, resulting in mechanical interlocking of the stent. This effectively restricts the rotating wire mechanism and increases the crush resistance of the stent significantly. These changing conditions can also influence the fatigue life of the stent. From the perspective of the tissue, the load distribution on the vessel wall is also affected; a deforming stent will transfer a part of the load to the tissue. Hence, when considering device-tissue interaction mechanisms, the adaptation of the tissue over time also needs to be taken into account.

CRediT authorship contribution statement

René Ubachs: Methodology, Writing – review & editing, Writing – original draft, Validation, Investigation, Formal analysis, Conceptualization. **Olaf van der Sluis:** Writing – review & editing, Supervision, Methodology, Conceptualization. **Scott Smith:** Writing – review & editing, Validation, Methodology, Investigation. **Jake Mertens:** Writing – review & editing, Validation, Methodology, Conceptualization.

Declaration of competing interest

The authors declare that they have no known competing financial interests or personal relationships that could have appeared to influence the work reported in this paper.

Data availability

No data was used for the research described in the article.

Appendix. Parametric stent model

For clockwise wire the following holds:

$$\theta = \frac{4\pi P}{25.4N} z \tag{A.1}$$

$$r = \frac{D}{2} + \frac{d}{2}\cos\left(\frac{N}{2}\theta\right) \tag{A.2}$$

To create a closed loop the above equations describe the stent for $z > h/2$, where h is the distance between wire crossings in axial direction: $h = 25.4/P$. For $z < h/2$ parabolic closing loops are created with the following equations:

$$0 < \theta < \frac{4\pi}{N} \tag{A.3}$$

$$r = \frac{D}{2} + \frac{d}{2}\cos\left(\frac{N}{4}\theta + \frac{\pi}{2}\right) \tag{A.4}$$

$$z = \frac{25.4N}{4\pi P}\left(\frac{N}{4\pi}\theta^2 + \frac{\pi}{N}\right) \tag{A.5}$$

References

Auricchio, F., Conti, M., De Beule, M., De Santis, G., Verhegghe, B., 2011. Carotid artery stenting simulation: From patient-specific images to finite element analysis. Med. Eng. Phys. 33 (3), 281–289. http://dx.doi.org/10.1016/j.medengphy.2010.10.011, URL: https://linkinghub.elsevier.com/retrieve/pii/S1350453310002420.

Brass, M., Kassab, G.S., 2019. Iliac veins are more compressible than iliac arteries: A new method of testing. J. Biomech. Eng. 141 (9), 091005. http://dx.doi.org/10.1115/1.4044227, URL: https://asmedigitalcollection.asme.org/biomechanical/article/doi/10.1115/1.4044227/955406/Iliac-Veins-Are-More-Compressible-Than-Iliac.

Clauwaert, T., 2012. Virtual and Experimental TAVI Bench Testing (Ph.D. thesis). Universiteit van Gent.

Conti, M., 2007. Finite Element Analysis of Self-Expanding Braided Wirestent (Ph.D. thesis). Universita' degli Studi di Pavia, Gent University.

Dabir, D., Feisst, A., Thomas, D., Luetkens, J.A., Meyer, C., Kardulovic, A., Menne, M., Steinseifer, U., Schild, H.H., Kuetting, D.L.R., 2018. Physical properties of venous stents: An experimental comparison. Cardiovasc. Intervent. Radiol. 41 (6), 942–950. http://dx.doi.org/10.1007/s00270-018-1916-1, URL: http://link.springer.com/10.1007/s00270-018-1916-1.

Gijsen, F., Katagiri, Y., Barlis, P., Bourantas, C., Collet, C., Coskun, U., Daemen, J., Dijkstra, J., Edelman, E., Evans, P., van der Heiden, K., Hose, R., Koo, B.-K., Krams, R., Marsden, A., Migliavacca, F., Onuma, Y., Ooi, A., Poon, E., Samady, H., Stone, P., Takahashi, K., Tang, D., Thondapu, V., Tenekecioglu, E., Timmins, L., Torii, R., Wentzel, J., Serruys, P., 2019. Expert recommendations on the assessment of wall shear stress in human coronary arteries: existing methodologies, technical considerations, and clinical applications. Eur. Heart J. 40 (41), 3421–3433. http://dx.doi.org/10.1093/eurheartj/ehz551, URL: https://academic.oup.com/eurheartj/article/40/41/3421/5576147.

Giuliodori, A., Hernández, J.A., Fernandez-Sanchez, D., Galve, I., Soudah, E., 2021. Numerical modeling of bare and polymer-covered braided stents using torsional and tensile springs connectors. J. Biomech. 123, 110459. http://dx.doi.org/10.1016/j.jbiomech.2021.110459, URL: https://linkinghub.elsevier.com/retrieve/pii/S0021929021002396.

Jedwab, M.R., Clerc, C.O., 1993. A study of the geometrical and mechanical properties of a self-expanding metallic stent—theory and experiment. J. Appl. Biomater. 4 (1), 77–85. http://dx.doi.org/10.1002/jab.770040111, URL: https://onlinelibrary.wiley.com/doi/10.1002/jab.770040111.

Jenei, C., Balogh, E., Szabó, G.T., Dézsi, C.A., 2016. Wall shear stress in the development of in-stent restenosis revisited. A critical review of clinical data on shear stress after intracoronary stent implantation. Cardiol. J. 23 (4), 9.

Kim, J.H., Kang, T.J., Yu, W.-R., 2008. Mechanical modeling of self-expandable stent fabricated using braiding technology. J. Biomech. 41 (15), 3202–3212. http://dx.doi.org/10.1016/j.jbiomech.2008.08.005, URL: https://linkinghub.elsevier.com/retrieve/pii/S0021929008004193.

Lally, C., Dolan, F., Prendergast, P., 2005. Cardiovascular stent design and vessel stresses: a finite element analysis. J. Biomech. 38 (8), 1574–1581. http://dx.doi.org/10.1016/j.jbiomech.2004.07.022, URL: https://linkinghub.elsevier.com/retrieve/pii/S0021929004003756.

Loo, K.V., 2006. Modellering en simulatie van zelfexpandeerbare draadstents (Ph.D. thesis). Universiteit van Gent.

Ma, D., Dargush, G.F., Natarajan, S.K., Levy, E.I., Siddiqui, A.H., Meng, H., 2012. Computer modeling of deployment and mechanical expansion of neurovascular flow diverter in patient-specific intracranial aneurysms. J. Biomech. 45 (13), 2256–2263. http://dx.doi.org/10.1016/j.jbiomech.2012.06.013, URL: https://linkinghub.elsevier.com/retrieve/pii/S0021929012003454.

May, R., Thurner, J., 1957. The cause of the predominantly sinistral occurrence of thrombosis of the pelvic veins. Angiology 8 (5), 419–427. http://dx.doi.org/10.1177/000331975700800505, URL: http://journals.sagepub.com/doi/10.1177/000331975700800505.

Murphy, E.H., 2019. Surveying the 2019 venous stent landscape. Endovasc. Today 18 (7).

Shanahan, C., Tiernan, P., Tofail, S.A., 2017a. Looped ends versus open ends braided stent: A comparison of the mechanical behaviour using analytical and numerical methods. J. Mech. Behav. Biomed. Mater. 75, 581–591. http://dx.doi.org/10.1016/j.jmbbm.2017.08.025, URL: https://linkinghub.elsevier.com/retrieve/pii/S1751616117303673.

Shanahan, C., Tofail, S.A., Tiernan, P., 2017b. Viscoelastic braided stent: Finite element modelling and validation of crimping behaviour. Mater. Des. 121, 143–153. http://dx.doi.org/10.1016/j.matdes.2017.02.044, URL: https://linkinghub.elsevier.com/retrieve/pii/S026412751730179X.

Wang, R., Ravi-Chandar, K., 2004a. Mechanical response of a metallic aortic stent—Part I: Pressure-diameter relationship. J. Appl. Mech. 71 (5), 697–705. http://dx.doi.org/10.1115/1.1782650, URL: https://asmedigitalcollection.asme.org/appliedmechanics/article/71/5/697/471554/Mechanical-Response-of-a-Metallic-Aortic-StentPart.

Wang, R., Ravi-Chandar, K., 2004b. Mechanical response of a metallic aortic stent—Part II: A beam-on-elastic foundation model. J. Appl. Mech. 71 (5), 706–712. http://dx.doi.org/10.1115/1.1782912, URL: https://asmedigitalcollection.asme.org/appliedmechanics/article/71/5/706/471566/Mechanical-Response-of-a-Metallic-Aortic-StentPart.

Ye, K., Lu, X., Li, W., Huang, Y., Huang, X., Lu, M., Jiang, M., 2012. Long-term outcomes of stent placement for symptomatic nonthrombotic iliac vein compression lesions in chronic venous disease. J. Vasc. Interv. Radiol. 23 (4), 497–502. http://dx.doi.org/10.1016/j.jvir.2011.12.021, URL: https://linkinghub.elsevier.com/retrieve/pii/S1051044311016393.

Zaccaria, A., Migliavacca, F., Pennati, G., Petrini, L., 2020. Modeling of braided stents: Comparison of geometry reconstruction and contact strategies. J. Biomech. 107, 109841. http://dx.doi.org/10.1016/j.jbiomech.2020.109841, URL: https://linkinghub.elsevier.com/retrieve/pii/S0021929020302645.

Zaccaria, A., Pennati, G., Petrini, L., 2021. Analytical methods for braided stents design and comparison with FEA. J. Mech. Behav. Biomed. Mater. 119, 104560. http://dx.doi.org/10.1016/j.jmbbm.2021.104560, URL: https://linkinghub.elsevier.com/retrieve/pii/S1751616121002423.

Záhora, J., Bezrouk, A., Hanuš, J., 2007. Models of stents – Comparison and applications. Physiol. Res. 56, http://dx.doi.org/10.33549/physiolres.931309.